Thermal Decomposition of Tricresyl Phosphate on Ferrous Surfaces

Arash Khajeh,[†] Fakhrul Hasan Bhuiyan,[†] Jon-Erik Mogonye,[‡] Rose A Pesce-Rodriguez,[‡] Stephen Berkebile,[‡] and Ashlie Martini[*,†]

[†]*Department of Mechanical Engineering, University of California Merced*

[‡]*U.S. Army Research Laboratory, Aberdeen Proving Ground*

E-mail: amartini(at)ucmerced.edu

Abstract

Tricresyl phosphate (TCP) forms protective films on moving mechanical components through thermally driven decomposition and interactions with the ferrous surfaces of the components. These reactions are hidden from view in moving interfaces, but are known to be sensitive to both the surface material and the isomeric form of the TCP. Here, temperature-programmed reaction spectroscopy (TPRS) and gas chromatography-mass spectroscopy (GC-MS) are complemented by reactive molecular dynamics (MD) simulations to investigate the thermal decomposition of meta and para isomers of TCP reacting with ferrous materials. Key observations are that the primary decomposition product of TCP is cresol, more cresol is generated on Fe_2O_3 than on Fe_3O_4, and that para-TCP isomers are more reactive than meta-TCP isomers. These trends are explained using the simulations to identify multiple reaction pathways leading to cresol formation. The likelihood of each pathway is quantified and correlated to surface material and TCP isomer trends in terms of energy barriers for the rate-limiting steps in the decomposition reactions.

Introduction

Phosphate esters are relevant to many different applications and used primarily as surfactants.[1] They are also used in the automotive and aviation industries as lubricant additives, where they protect moving mechanical components from wear in extreme conditions.[2–4] One of the most widely used and extensively studied phosphate ester lubricant additive is tricresyl phosphate (TCP). TCP functions as an anti-wear additive by reacting with ferrous surfaces to form protective films, called tribofilms. Characterization of these films has shown that they can be comprised of iron phosphate,[5,6] organic polyphosphates[7] or iron polyphosphate.[8,9] Further, multiple mechanisms for the conversion of TCP into a tribofilm have been proposed, including the formation of phosphoric acid through hydrolysis of the TCP, adsorption of TCP on the surface followed by thermal decomposition, and adsorption followed by

decomposition through a nucleophilic attack by other surface-adsorbed species.[2,10] Consistent across all of these mechanisms is the decomposition of the TCP.[3] However, a challenge to understanding the decomposition reaction pathways leading to TCP tribofilm formation is that the reaction rates and products are dependent on multiple factors.[11]

Film formation reactions from TCP and other phosphate esters have been characterized indirectly, using friction or wear measurements as a proxy for film growth, or directly using various experimental characterization techniques. Commonly used direct approaches involve identifying organic compounds produced from thermal decomposition in the gas phase using, for example, gel permeation chromatography (GPC),[8,12] temperature programmed desorption (TPD)[13–16] and gas chromatography-mass spectroscopy (GC-MS).[6,8,9] Such techniques quantify reactivity from the abundance of gaseous compounds and the lowest temperature at which they are observed. These methods also identify reaction products, and prior studies have shown that the primary products of TCP decomposition are tolyl-TCP, cresol and higher molecular weight species.[2,8,9,15,17]

Atomistic simulations have been used to study this topic as well.[10,18–22] Since decomposition and film formation reactions involve the formation and breaking of chemical bonds, the three relevant simulation methods are density functional theory (DFT), *ab initio* molecular dynamics (AIMD) simulation, and reactive molecular dynamics (MD) simulation. These tools can mimic experiments by modeling heating processes and tracking the rate of reaction product formation. However, their strength lies in the ability to demonstrate reaction pathways, including intermediates that may not be detectable using experimental methods. Here, we focus on the use of the experimental and computational tools to characterize the effect of the surface and the molecular species on thermal decomposition reactions of phosphate esters, with emphasis on TCP and ferrous surfaces.

Decomposition reactions leading to film formation are necessarily affected by the nature of the surface itself. For example, TCP was found to exhibit better anti-wear performance on nitrided and oxy-nitrided surfaces compared to sulfurized steels.[23] Another comparison of

TCP reactivity on different surfaces in vapor-phase lubrication showed that decomposition rates on iron and copper were relatively fast, but were slower for quartz, nickel, and tungsten.[11,24] A comparison of gold and iron showed that TCP physisorbed and then desorbed at higher temperatures on inert gold surfaces but decomposed and formed a film on ferrous surfaces.[25] A study that included both commercial-grade TCP and pure TCP isomers found that reactivity on various metals/oxides increased with increasing surface oxidation state.[8] That study also showed that different types of steel exhibited different levels of reactivity, with 316C stainless steel being the least active. The difference in reactivity between ferrous surfaces is particularly important since the surfaces of lubricated mechanical components have been reported to be chemically heterogeneous and comprise multiple iron oxides.[26–28]

Experimental studies on the effect of surfaces have been complemented by reactive MD simulations that showed that C–O dissociation reactions in tri(n-butyl)phosphate and tri(s-butyl)phosphate proceed faster and at lower temperatures on α-Fe(110) than Fe_3O_4.[18] The same study also suggested that hydroxylation of the surface to form Fe_3O_4-OH further inhibited dissociation. In contrast, P–O dissociation was faster on the Fe_3O_4 than the α-Fe(110) surface. This result, which was consistent with the experimental observation of more reactivity on iron oxide,[8] was explained by the need for oxygen atoms on the surface to enable P–O scission via nucleophilic substitution.[18] Other reactive MD simulations of thermal decomposition of TCP on Fe_3O_4-OH showed that the dominant reaction pathway involved Fe–C bonding.[19] These reactions were then shown to be accelerated by the presence of nanodiamonds on the surface in both simulations and quartz crystal microbalance experiments.[20]

In addition to surfaces, the rates of dissociation reactions depend on the chemistry and structure of the molecular species. GPC was used to compare TCP to three alkyl phosphates, which showed that the TCP decomposed at a higher temperature than any of the alkyl phosphates.[12] Similarly, the decomposition temperature of TCP on steel measured by X-ray photoelectron spectroscopy[25] was higher than that for tributyl phosphate on iron ox-

ide measured using TPD.[16] A study that included commercial-grade TCP and three pure TCP isomers (para–p, meta–m, ortho–o) showed that reactivity characterized by GPC was sensitive to the type of TCP and surface.[8] Specifically, on Fe_2O_3 surfaces, it was found that reactivity increased as commercial TCP $\approx$ ortho < meta $\approx$ para; on Fe^0, reactivity increased as ortho < meta $\approx$ para $\approx$ commercial TCP.[8] In another study, GC-MS experiments performed between 673 and 723 K showed a larger number of decomposition products for para-TCP than meta-TCP.[29] The decomposition products for both TCP isomers were then shown to be dependent on the availability of a metal surface and oxygen.

The effect of reactant chemistry has also been explored using simulations. *Ab initio* MD simulations of trimethyl phosphite and tributyl phosphite confined and sheared between Fe(110) slabs showed that dissociation of both molecules proceeded along the same pathway at high load, but that more phosphorous was likely to be released with the smaller molecule because of the greater number of adsorbed molecules per unit area.[22,30] It was further shown that the energy of dissociation adsorption decreased as the number of detached methoxy groups increased.[31] Lastly, reactive MD simulations compared TCP with four alkyl phosphates (primary linear, primary branched, secondary, and tertiary).[18] Analysis of thermal decomposition on Fe_3O_4 showed that the onset temperature for C–O cleavage increased as tertiary < secondary < primary < TCP, indicating the tertiary alkyl was the most reactive, and this trend was explained by the relative stability of radicals formed by C–O dissociation. However, the P–O cleavage rate was faster for the primary alkyl than the other molecules, and this was explained by steric hindrance that inhibited nucleophilic attack by the surface oxygen.[18]

As the above review demonstrates, the rates and pathways of decomposition reactions leading to film formation depend on the reactant species and surfaces. However, trends are inconsistent across the different studies, possibly because most studies used just one experimental or simulation technique to quantify reactivity. Here, we combine two different experimental methods, temperature-programmed reaction spectroscopy (TPRS) and GC-

MS, with reactive MD simulations to explore thermal decomposition reactions of TCP on ferrous surfaces. We particularly focus on reactions between TCP and iron oxides, as these material systems are most relevant to lubricated mechanical components. Specifically, the experiments and simulations are combined to characterize the decomposition products and reactivity of three different ferrous surfaces – Fe with native oxide, Fe_2O_3 and Fe_3O_4 – and two isomers of TCP – meta and para. Results obtained using the various techniques are compared and contrasted. Finally, key trends that are consistent across the different methods are explained in terms of reaction pathways identified and quantified in the simulations.

Methods

Temperature-Programmed Reaction Spectroscopy

TPRS experiments were accomplished using a custom-built environmental chamber capable of high vacuum (<10 mTorr base pressure) or a controlled gas environment up to 1.1 atm. Air with relative humidity between 18% and 35% or nitrogen with a purity of 99.9% was introduced to the chamber after pumping to <10 mTorr for each experiment. A Hiden HPR-20 R&D atmospheric sampling quadrupole mass spectrometer was used to analyze the mass over ion charge of desorption products up to 300 m/z. Molecules were ionized with a hot-filament (emission current 250 µA) electron impact ionization source within the mass spectrometer with an ionization energy of 70 eV. The differentially-pumped inlet of the mass spectrometer was connected to the environmental chamber through a heated glass capillary suspended about 1 cm from the specimen with a specified response time of < 500 ms. In order to maintain a constant pressure in the environmental chamber, make-up air or nitrogen was leaked into the chamber to compensate for gas pumped by the mass spectrometer inlet. Any reacted and/or desorbed molecular species will therefore appear in the mass spectrometer signal as a peak with increasing temperature because molecules are continually depleted from the chamber gas at a constant rate. As the species is released from the specimen,

the signal rises with increasing concentration in the chamber gas, indicating the start of reaction/desorption. As desorption slows with temperature increase and surface reactant consumption, the signal peaks when desorption equals depletion rate from the chamber. Once desorption completes at higher temperature, the chamber concentration then drops back below detectable limits.

Powders of Fe (99.997%), Fe_2O_3 (99.99%), or Fe_3O_4 (99.997%) from AlfaAesar were placed in a 1-cm diameter flat-bottomed borosilicate glass vial which had been cleaned for 10 min in an air plasma cleaner. The mass of powder used was 20 mg for Fe, and 13 mg for Fe_2O_3 and Fe_3O_4, which should correspond to roughly the same surface area assuming similar particle size distributions. No mass signal was observed at 2, 91, 108, and 165 m/z from dry powders heated to over 750 K. 1 µL TCP (mixture of meta- and para-isomers, <1% ortho-isomer, SYN-O-AD 8484 from ICL-IP America, Inc.) was dissolved in 50 µL of anhydrous ethanol (99.9%), then placed in drops with a pipette directly onto the powder. The ethanol was then allowed to evaporate completely in the air or under vacuum until no ethanol signal was observed in the mass spectrometer. The vial was placed on a resistively heated ceramic heater surface about 1 cm beneath the orifice of the heated glass capillary.

Temperature was monitored at the bottom surface of the glass vial embedded in the powder with a K-type thermocouple. Temperature ramps were begun at 303 K with a heating rate of 0.25 K/s to allow for even heating of the powder. TCP (368 m/z) evaporated into the mass spectrometer was seen to correlate with a significant signal at 165 m/z as the most prominent and highest mass fragment, and signals at 91 m/z and 108 m/z from toluene and cresol, respectively, due to fragmentation of the TCP in the mass spectrometer. Relative sensitivities of 6.8 for 91 m/z, and 1.0 for 108 and 165 m/z were used in the mass spectrometer signal. The ratio of 91 m/z:165 m/z was 0.621, and 108 m/z:165 m/z was 0.124 from the pure TCP signal, according to the NIST Chemistry Webbook.[32] Contributions due to fragmentation of TCP molecules that reached the detector were removed by subtracting the signal of 165 m/z multiplied by these ratios from the signal of 91 and 108 m/z so that

the resulting data only represents toluene and cresol that desorbed as such from the sample. Fig. 1 illustrates the molecular structures of mmm-TCP, ppp-TCP and their fragments.

Gas Chromatography – Mass Spectrometry

Pyrolysis products were analyzed by means of a gas GC-MS instrument with a desorption interface. Desorption was achieved via a CDS Analytical Model 2000 Pyroprobe (coil type) connected through a heated interface chamber to the splitless injector of an Agilent (Santa Clara, California) GC/MS system (Model 6890N GC and Model 5973N MSD). The GC column used was a HP-5 capillary column (0.25 mm $\times$ 30 m, 0.25-µm film). The injector temperature was 523 K; the Pyroprobe interface was set to a temperature of 523 K. The GC oven temperature program was as follows: 373 K isothermal for 1 min, 373–523 K at 40 K/min, and 523 K isothermal for 1 min. The Pyroprobe was programmed to give a 20-s desorption pulse at 523 K at a heating rate of 1,000 K/s. The pulse temperature is based on calibration provided by the vendor and was not measured for this study. Samples consisted of approximately 2 mg of Fe, Fe_2O_3 or Fe_3O_4 plus 1 uL of TCP solution (100 µl TCP in 1mL ethanol). TCP solution was applied directly by syringe to a solid substrate that was pre-loaded into a quartz tube. Neat TCP was analyzed by applying the solution to glass wool. The quartz tube containing the sample was then placed in the coils of the Pyroprobe, which was then inserted into the Pyroprobe interface.

Reactive Molecular Dynamics Simulations

The molecular dynamics simulations captured TCP molecules interacting with Fe_3O_4 and Fe_2O_3 surfaces (snapshots in Fig. S1). Atomic interactions were modeled using the ReaxFF[33] force field with a parameter set previously developed for Fe/P/O/C/H. This parameter set has been shown to accurately reproduce P and PO adsorption energies on Fe(001)[19] as well as the adsorption and dissociation energies of intact and dissociated tri(n-butyl)phosphate on α-Fe(100)[18] by comparison to energies calculated using DFT. All simulations were run using

8

the large-scale atomic/molecular massively parallel simulator (LAMMPS)[34] with a timestep of 0.25 fs. The temperature was controlled using a Nosé-Hoover thermostat applied to the free atoms. Post-processing of results was carried out using Python scripts and OVITO software.[35]

To construct the model systems, first, crystalline unit cells of Fe_2O_3 and Fe_3O_4 were created and duplicated in the [100], [010] and [001] directions using QuantumATK.[36] The crystalline slabs of material were then annealed to create disordered surfaces. The annealing process consisted of heating from 300 K to 4000 K over 25 ps, equilibration at 4000 K for 125 ps, and then cooling to 300 K over 500 ps, following a procedure used previously for the creation of amorphous Fe_3O_4 surfaces.[18,19] Next, the slabs were truncated from the bottom such that they were all the same size: 2.5 nm × 2.5 nm in the plane of the surface and 2.0 nm thick. The positions of the atoms in the bottommost 0.3 nm of the slabs were fixed to approximate the bulk of the material. Periodic boundary conditions were applied in the plane of the surface, and a non-periodic boundary condition was used in the vertical direction.

The amorphous substrates were next passivated by hydroxylation. For this process, 300 water molecules were placed above the substrates, and the temperature was set to 700 K for 750 ps to accelerate reactions. Then the system was cooled down to 300 K, after which any atoms not covalently bonded to the surface were removed. After passivation, the surfaces were extended in the two directions parallel to the surface and truncated from the bottom to have a final dimension of 5 nm × 5 nm × 1.3 nm (length × width × thickness).

Once the surface models were complete, 64 TCP molecules were placed at random positions and orientations above the surface, starting ≈ 0.5 nm from the topmost surface atoms. The simulation was started with energy minimization, followed by thermal equilibration at 300 K for 100 ps. A repulsive wall was placed at the height of 5.4 nm to prevent atoms from leaving the simulation box. The temperature was increased from 300 K to 700 K at a fixed heating rate of 0.1 K/ps, and then further increased to 1700 K at a heating rate of

1 K/ps. The slower heating rate at the beginning was applied to provide the system with enough time for adsorption reactions to take place. The higher heating rate was applied to accelerate desorption.

Simulations were performed for the two surfaces, Fe_2O_3 or Fe_3O_4, and TCP having three meta-cresol substituents (mmm) or TCP with three para-cresol substituents (ppp). Two independent simulations were run for each of the four surface/isomer combinations. Results were analyzed in terms of the type and number of chemical species observed during the desorption stage of the simulations. Snapshots of mmm-TCP and ppp-TCP molecules as well as cresol and toluene decomposition products are shown in Fig. 1.

Nudged Elastic Band

Nudged Elastic Band (NEB) [37–39] calculations were performed to compute the energy barriers for different reaction pathways. NEB was implemented using LAMMPS with the same ReaxFF potential as described above for the dynamic simulations. The NEB method enables calculation of the Minimum Energy Path (MEP) for any transition and has been used to compute energy barriers for various reactions, including adsorption, desorption, and decomposition. [40,41] In the NEB calculations performed here, 24 number of replicas were used, including the initial and final replicas. The initial and final states were taken directly from the reactive simulation and the intermediate replicas were initially created via linear interpolation.

All the replicas were connected by springs to ensure the replicas would be equally spaced. The total force acting on a replica was the sum of the spring force along the tangent and the true force perpendicular to the tangent. [38] The series of replicas converged to the MEP by minimizing the total force acting on each of the replicas by damped dynamics. [39] The climbing image method was also incorporated in the NEB calculations, where the replica with the highest energy is detected after the regular NEB minimization and is driven to the top of the energy barrier to maximize its energy. [42] This improved the resolution of the energy
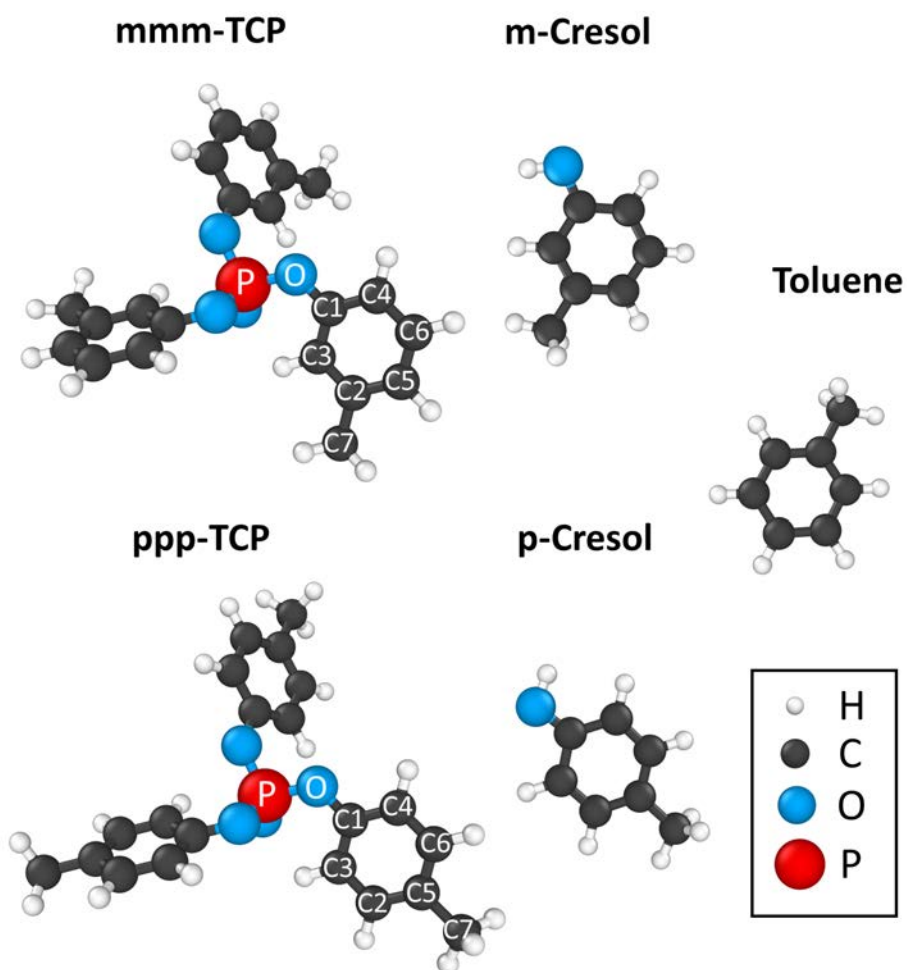
10

Figure 1: Snapshots of atomistic models of mmm-TCP, ppp-TCP, m-cresol, p-cresol and toluene. The atoms in the TCP are numbers according to their position in the structure.

profile near the saddle point and prevented the saddle point replica from slipping down from the high energy regions towards the minima. A perpendicular spring with a spring constant ranging from 100 to 50,000 Kcal/(mol.Å^2) was also employed until a force criterion of 0.9 kcal/(mol.Å) was met for the saddle point.

Results

The result of the TPRS experiments performed with TCP on Fe, Fe_3O_4, and Fe_2O_3 powders are shown in Fig. 2 for a temperature ramp rate of 0.25 K/s in air and in dry nitrogen gas environments. In the air (Fig. 2a), cresol (108 m/z) was the most prominent desorption product by two orders of magnitude, as indicated by the relative signal strength (note multiplication factor of x2.2 for cresol to x94 for toluene). In both Fe and Fe_2O_3 powder, desorption of cresol began at around 450 K with a peak at 520 K, although significantly more product was desorbed for Fe. In Fe_3O_4 powder, desorption of cresol began around 475 K and peaked around 530 K with less than half of the peak area of the Fe powder. Toluene desorbed around 515 K for the Fe powder, but no clear toluene signal was detected for either of the oxide powders. No TCP desorption was observed in any of the powders in the air.

In a nitrogen gas environment at a ramp rate of 0.25 K/s (Fig. 2b), cresol was again the greatest desorption product, by over one order of magnitude. Fe had an onset desorption temperature for cresol of 550 K with two peaks at 590 K and 640 K, while cresol from Fe_2O_3 had the same onset and peak temperatures with a markedly larger higher temperature peak. Cresol from Fe_3O_4 had a lower temperature onset of around 500 K and a peak at 575 K. In contrast to the air environment, the cresol peak from Fe_2O_3 had the largest area of the three powders in the nitrogen environment. The areas of the cresol peaks from Fe_3O_4 and Fe were similar to each other. A small amount of toluene was produced from all three powders at around 575 K. TCP was also observed to desorb with peaks at 550 K for Fe_3O_4, and 580 K for Fe and Fe_2O_3.

The results of GC-MS experiments performed on the three different iron-based substrates and neat TCP are shown in Fig. 3. Fig. 3(a) displays the selected ion chromatogram (SIC) for a MS signal of m/z = 107, which corresponds to cresol, for neat TCP and TCP reacted with Fe, Fe_2O_3 and Fe_3O_4. A MS signal from toluene was not observed. The earlier signal in Fig. 3(a) starting at around 4 min retention time resulted from cresol molecules released from the specimens directly. TCP mixed with the three iron-based powders released cresol
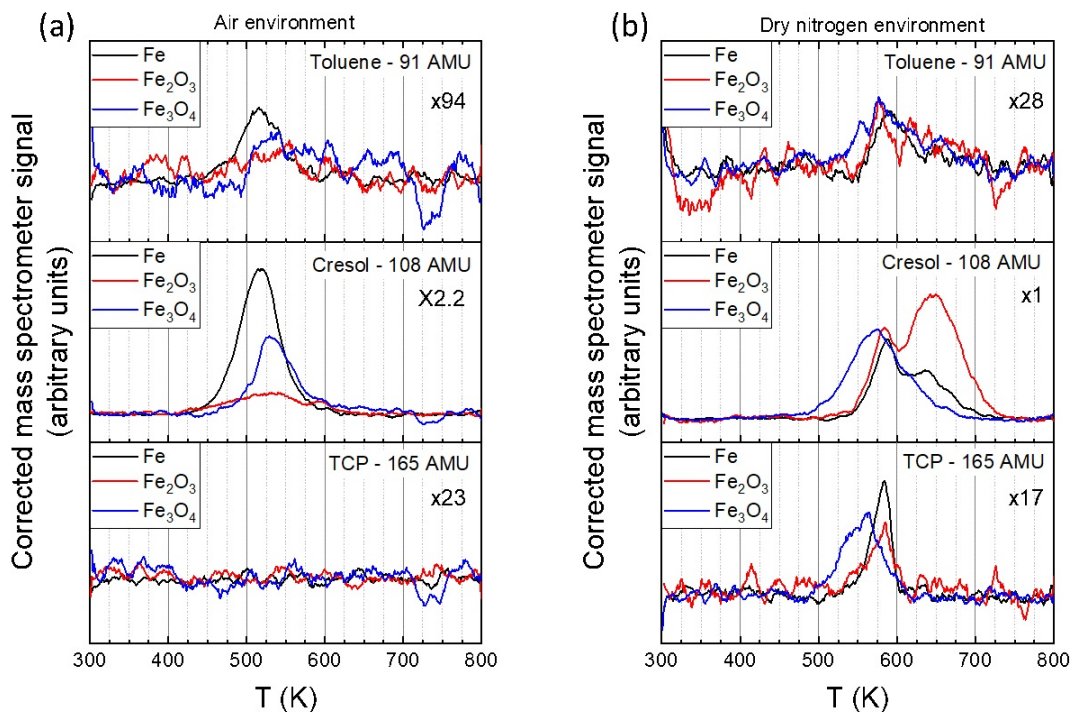
Figure 2: Thermal programmed reaction spectroscopy of TCP on Fe, Fe_2O_3, and Fe_3O_4 with a heating rate of 0.25 K/s in (a) an air environment and (b) a dry nitrogen environment. Masses 91, 108, and 165 m/z, top to bottom in each panel, correspond to toluene, cresol, and TCP. Cresol and toluene contributions from TCP cracking products in the mass spectrometer have been removed. Signal strength relative to cresol in dry nitrogen is indicated.

which appeared at retention times beginning around 3.8 minutes, increasing to a peak at about 4.0 minutes (or shoulder for Fe_3O_4), then a second peak at 4.4 minutes, before trailing off over the next two minutes. The signals from the three powders differed in shape, but were similar in magnitude (note the decrease in abundance signal scale from the TCP neat down to the TCP + Fe_2O_3). The results of the iron powders contrasted with the behavior of neat TCP that produced cresol with a retention time of 4.2 minutes to peak at 4.4 minutes before trailing off. The intensity of cresol from neat TCP was about four times less than the cresol produced by the powders.

The later signals in Fig. 3(a) resulted from TCP molecules that desorbed from the specimens whole, and were then fragmented in the electron impact ionization section of the mass spectrometer. Here, four peaks were observed at retention times of 9.3, 9.5, 9.7, and 9.9

minutes for the three powders and from neat TCP. These peaks correspond to the four iso-mers present in the TCP, i.e. TCP with three meta-cresol substituents (mmm), TCP with two meta- and one para-cresol substituents (mmp), TCP with one meta- and two para-cresol substituents (mpp), and TCP with three para-cresol substituents (ppp), from low to high retention times in the GC. Fig. 3(b) shows the peak area of the four isomers from Fig. 3(a), normalized to the meta-meta-para isomer peak area. From the GC-MS peak areas of the neat TCP, the isomer distribution ratio observed is roughly 1:3:3:1 mmm:mmp:mpp:ppp, with a slightly higher abundance of the meta-containing isomers. Key observations are that the normalized peak area is lower for the ppp-TCP than the mmm-TCP (and similarly lower for mpp than mmp) and, comparing the different powders, the abundance of desorbed TCP is highest for neat TCP, then decreases progressively for Fe_3O_4 to Fe to over an order of magnitude lower for Fe_2O_3.
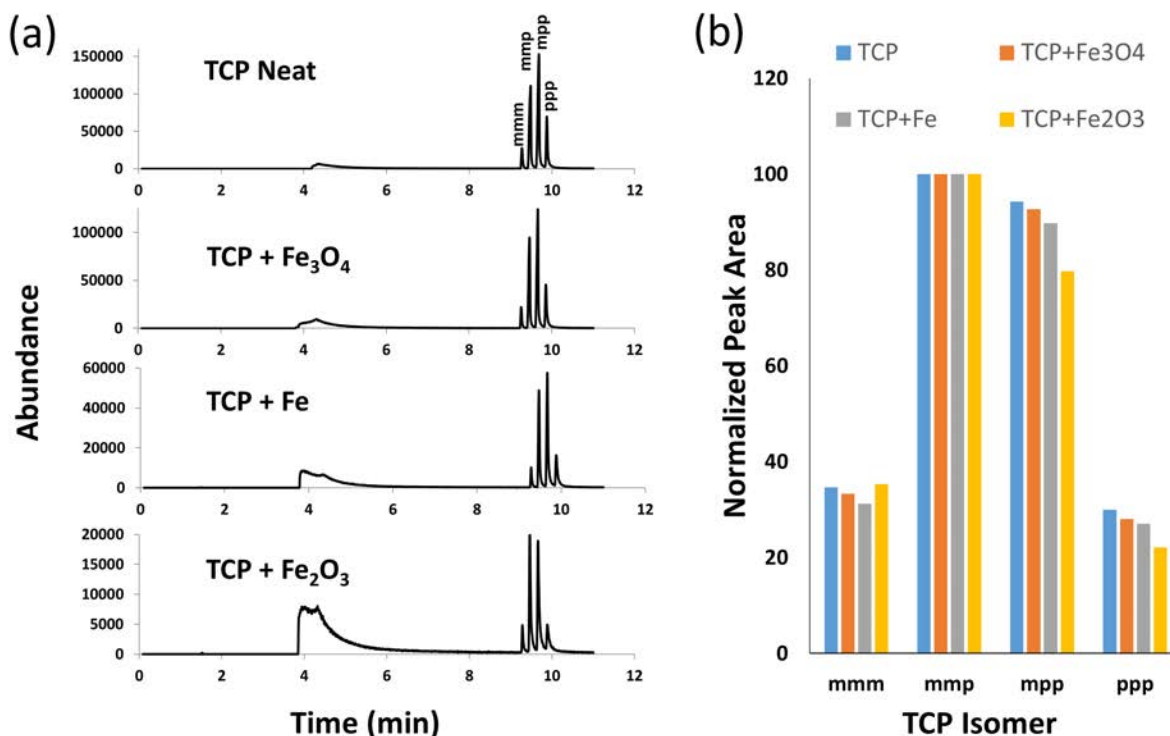

Figure 3: Figure 2: (a) GC-MS SIC for a MS signal of m/z = 107 corresponding to cresol for neat TCP and TCP reacted with Fe, Fe_2O_3 and Fe_3O_4. (b) Normalized GC-MS peak areas for the different TCP isomers from 9 to 10 minutes retention time in (a).

14

Results from reactive MD simulations of mmm-TCP and ppp-TCP isomers on Fe_3O_4 and Fe_2O_3 surfaces are shown in Fig. 4. Consistent with the TPRS and GC-MS experiments, there is little toluene produced. Instead, the primary reaction products are cresol, tolyl-TCP, and higher molecular weight species (subsequently referred to as oligomers) resulting from bonding between TCP and/or radicals generated by TCP decomposition.

We specifically analyzed the cresol, since this was the primary reaction product observed in the experiments. The results in Fig. 4 do not show any statistically significant differences between the amount of cresol formed on the two oxide surfaces. To compare the reactivity on the two oxide surfaces, the number of cresols formed from mmm- and ppp-TCP are shown in Fig. S3(a) for Fe_3O_4 and Fig. S3(b) for Fe_2O_3. This figure shows that, in all cases, the rate of cresol generated significantly increases after the formation of the first two cresol species (see the horizontal dash line on Fig. S3). The temperature corresponding to this increase was found to be lower for ppp-TCP than mmm-TCP (850 K on Fe_3O_4 and 1250 K on Fe_2O_3 for ppp-TCP vs. 1175 K on Fe_3O_4 and 1425 K on Fe_2O_3 for mmm-TCP). Further, the number of p-cresol is consistently higher than the number of m-cresol, on both surfaces and at any temperature (averaged over time, four more p-cresol than m-cresol, see Fig. S3).

Note that there are several key differences between the MD and experiments. First, the TPRS and GC-MS spectra exhibit peaks due to the reaction rate increases with temperature leading to more desorption followed by a decrease in desorption products due to lack of availability of reactants on the surface. The decrease cannot be captured in the simulations because of the finite size of the model and the fact that the reaction products do not leave the simulation domain after desorption. Also, desorption in the TPRS measurements starts around 450 K, which is significantly lower than the formation temperature in the simulations (1000 K). This quantitative mismatch is attributable to the much faster heating rate in MD compared to experiments.[18,21,43] Faster heating rates allow for less time at critical temperatures and so cause higher desorption temperatures.[44–46]

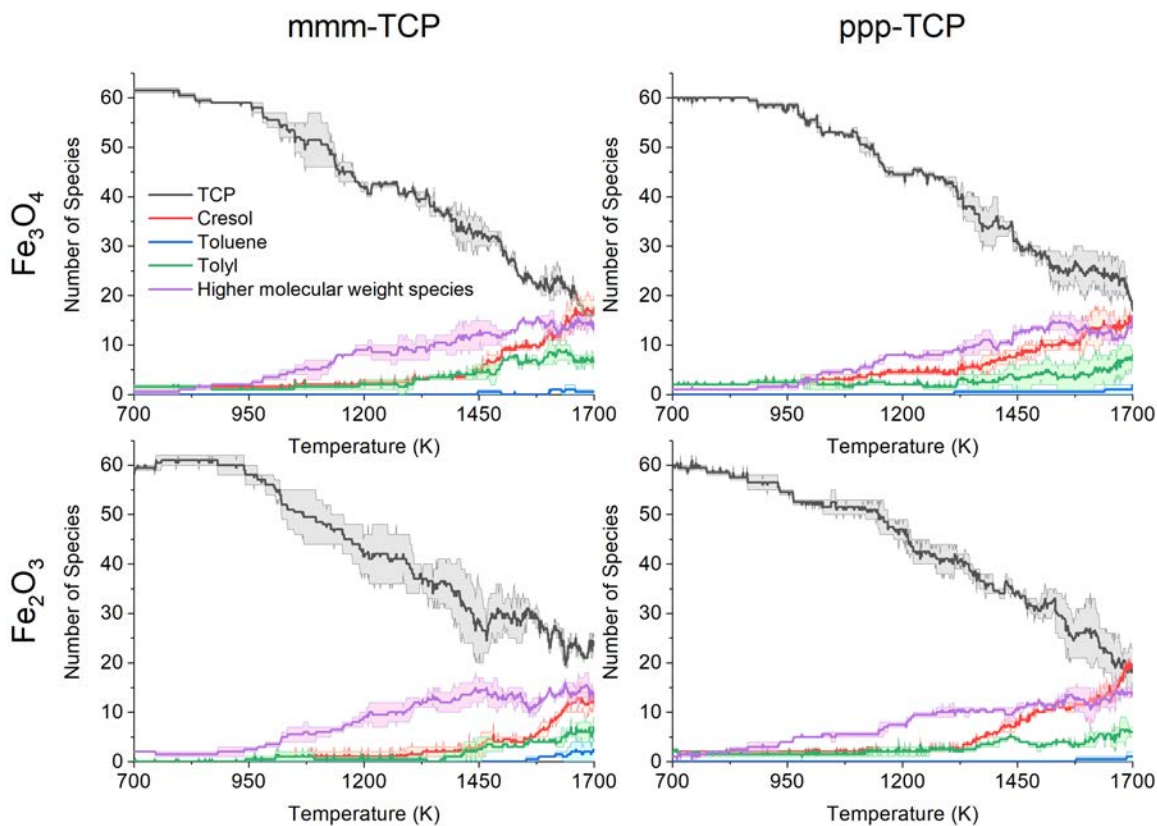Regardless of their differences, the results from two different experimental methods and

Figure 4: Number of chemical species as a function of temperature observed from simulations of desorption for mmm-TCP and ppp-TCP on Fe_3O_4 and Fe_2O_3 surfaces. Lines are averages of two independent simulations and shaded regions reflect the standard error of the two independent simulations.

MD simulations reveal several key trends. First, a primary reaction product of thermal decomposition of TCP was cresol in the TPRS and GC-MS experiments as well as in the simulations. Also, both simulations and GC-MS experiments show that the para-TCP isomer is more reactive than the meta-TCP isomer on both Fe_3O_4 and Fe_2O_3. Lastly, regarding the role of surface chemistry, GC-MS experiments suggested higher reactivity of TCP on Fe_2O_3 than Fe_3O_4.

Discussion

Analysis of Observed Experimental Trends

In TPRS, the most prominent desorption product was cresol in both air and nitrogen environments. A small signal from toluene was observed only for Fe powders in air and for all three powders in N_2. Sung et al. demonstrated that mmm-TCP and mmm-cresol on single crystal Fe in vacuum both had desorption peaks of mmm-cresol at 285 to 315 K and 505 to 515 K, while a smaller amount of toluene desorption was detected around 345 and 500 K.[15] In the present experiments with powders, presumably any desorption around a temperature of 300 K was already complete before the ramp due to awaiting ethanol desorption at room temperature, and a starting temperature for the ramp of 303 K. The desorption temperature observed in the powders at higher temperatures was quite similar for mmm-cresol with peaks from 520 K to 650 K, despite nearly an order of magnitude difference in the ramp rates (Sung et al. used 2 K/s). Considering the greater surface area, spaces between the powder particles, and greater inhomogeneity of the powder surfaces, the desorption temperature could be expected to display a larger range of values for the present study. Further, as observed for the Fe single crystal, a small amount of toluene was produced in the Fe powder. However, the Fe powder produced significantly less toluene than the single crystal when compared to cresol, presumably due to some surface oxidization of the powder. Toluene was not detected for the oxide powders. It is significant that atomically clean Fe and air-exposed Fe and oxides both produce primarily cresol from TCP at similar temperatures, and that toluene production decreases with oxide content.

Another consequence of the lack of available oxygen in the environment appears to be a lower overall reactivity of the TCP on the powder surfaces. First, there was less consumption of the TCP by the powders, since a small TCP signal is present in the nitrogen environment. Concomitant with this TCP desorption, a cresol desorption (and very small toluene desorption) was observed. Second, the onset of the reaction and desorption of cresol

occurred at higher temperatures in the nitrogen environment of around 25 to 100 K higher for this concomitant signal. Therefore, the energy needed for the initial reaction was increased slightly in the nitrogen environment. Third, a second desorption of cresol occurred at higher temperatures in the nitrogen environment (but not in air), as represented by the second, higher temperature peak in the Fe_2O_3 and Fe signal and the extended shoulder in the Fe_3O_4 signal. This second reaction and desorption required additional thermal energy and may have originated from TCP that remained after the first reaction, perhaps through delay of one of the three cresol release pathways described in the simulations.

GC-MS results agree with the TPRS in that cresol is the main product released from the Fe, Fe_3O_4, and Fe_2O_3 powders. The earlier onset and intensities of the cresol retention peaks around 4 minutes indicate that significantly more cresol molecules were released from the powders than from neat TCP, and more readily. The intensity of the second set of retention peaks of desorbed TCP molecules with respect to the cresol retention peaks decreased from neat TCP to Fe_3O_4 to Fe to Fe_2O_3, indicating the increasing binding of the TCP molecules throughout this series. From the relative intensities of the second set of retention peaks within the grouping from each substrate, we can form some conclusions about the relative reactivity of the four isomers. When normalized to the "mmp" TCP isomer and then compared with neat TCP, two observation are made: isomers containing para-cresol are preferentially depleted relative to isomers containing meta-cresol and para-depletion depends on the substrate such that $Fe_2O_3 >$ Fe $> Fe_3O_4$. Based on XPS analysis of aged Fe surfaces by Olla,[28] it is clear that "exposed" Fe surfaces such as those used in the current investigation are comprised of not only Fe metal, Fe II and Fe III oxides (including Fe_2O_3 and Fe_3O_4), but also a significant level of FeO(OH). Under the conditions of our GC-MS analysis (i.e. 523 K), the temperature is sufficient to dehydrate FeO(OH) and convert it to Fe_2O_3,[47] thereby increasing the overall level of Fe_2O_3 on the surface of the Fe particles. While the level is certainly not as high as that on neat Fe_2O_3 particles, it is assumed to be significantly higher than that on the surface of Fe_3O_4 particles. Based on this assumption,

it is concluded that the preferential depletion of p-cresol TCP isomers (ppp and mpp) is correlated with Fe_2O_3 content on substrate surfaces. This finding is in general agreement with results of Saba and Forster[8] for tri-p-TCP with Fe_2O_3 and Fe, which showed Fe_2O_3 >> Fe when reacted at 748 K. While they did not investigate the reaction of ppp-TCP with Fe_3O_4, general conclusions from their study of tri-m-TCP reaction with Fe and Fe oxides suggest Fe_3O_4 to be more reactive than Fe to TCP. Given that Saba and Forster pre-heated their substrates at 723 K prior to exposure to TCP and the fact that that the surface of Fe would be expected to be mostly oxide, it is not clear why reaction rates of TCP with Fe powders should be different than with Fe oxides, unless the surfaces had been protected from oxidation. There is no mention that this was the case.

Reaction Pathways

The origins of the key trends discussed above were investigated using the atomic-scale details available from the simulations. First, the reaction pathways leading to cresol formation were identified. It was found that the decomposition of TCP leading to the formation of cresol proceeded via three primary pathways: hydroxylation, adsorption, and oligomerization. Snapshots of representative reactions are shown in Fig. 5. Direct dissociation of the TCP P–O bond due to thermal vibration was also observed at higher temperatures, but this occurred infrequently compared to the main three pathways.

The hydroxylation pathway shown in Fig. 5a began with water molecules and OH groups from the surface. Depending on the orientation and proximity of a TCP molecule to such water and OH groups, they could initiate a nucleophilic attack on the P atom of the TCP which would then undergo a hydroxylation reaction. Investigation of several hydroxylation cases suggest that the newly attached OH group weakens the other P–O bonds, eventually leading to P–O bond dissociation and the formation of cresol.

The adsorption pathway is illustrated in Fig. 5b. This pathway was initiated by reactions between C atoms in the cresol rings and Fe atoms on the surface as observed in previous
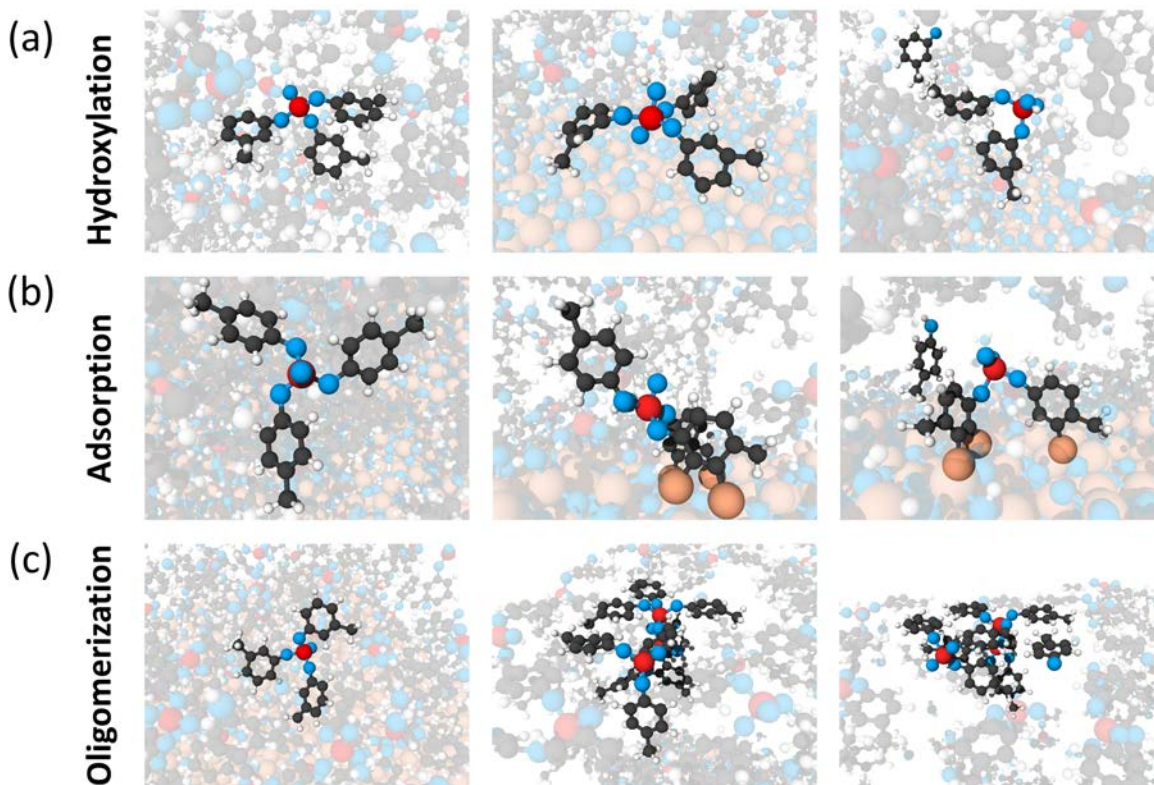
Figure 5: Snapshots of the key steps of the three cresol formation reaction pathways: (a) hydroxylation, (b) adsorption and (c) oligomerization. From left to right, the first images show the TCP molecule before reaction, and the last images show the dissociation of a P–O bond to form cresol. The adsorption snapshots were taken from a simulation of ppp-TCP on the Fe_3O_4 surface and the snapshots for the other two pathways were taken from a simulation of mmm-TCP on the Fe_2O_3 surface. The red, blue, black, white and brown spheres represent P, O, C, H and Fe atoms, respectively.

studies.[18–20] Then, one of the three P–O bonds broke to create a cresol molecule. The dissociated cresol could be the one that initially formed the Fe–C bond, or it could be one of the two other rings. The former case produced an adsorbed cresol as the remainder of the TCP moved away freely in the form of tolyl phosphate. The latter case, shown in Fig. 5b, produced a free cresol molecule, leaving the remainder of the TCP adsorbed on the surface. The adsorbed TCP molecule was sometimes hydroxylated before P-O bond dissociation.

Interactions between multiple TCP molecules or TCP and various radicals or other molecules resulted in the formation of higher molecular weight species. These oligomers containing between two to four P atoms and more than three cresol rings are consistent with

20

polymeric products observed in previous experiments.[2,8,9] Some of the oligomers lost one or more cresol rings to produce cresol in the system, as in the case shown in Fig. 5c. In some instances, the oligomers were also adsorbed on the surface through either Fe–C bonds or Fe–O bonds.

The relative frequency of each reaction pathway observed in the MD simulations was calculated. A summary of the reaction pathway statistics for mmm- and ppp-TCP on the two oxides is given in Table 1, where direct P–O dissociation refers to cresol formed not through one of the three primary pathways.

Table 1: Percent of the total cresol formation reactions that occurred via each of the identified pathways in the reactive MD simulations.

	mmm-TCP		ppp-TCP	
	Fe_2O_3	Fe_3O_4	Fe_2O_3	Fe_3O_4
Hydroxylation	43%	59%	39%	36%
Adsorption	5%	14%	7%	15%
Oligomerization	43%	24%	50%	46%
Direct P-O Dissociation	9%	3%	4%	3%

The relative frequency of the different reaction pathways in Table 1 can be correlated qualitatively to the different reactivity of the TCP isomers and oxide surfaces in experiments. First, the GC-MS results indicated Fe_2O_3 was more reactive than Fe_3O_4 in terms of cresol formation. In Fig. 5b, the first step of the adsorption pathway is the formation of Fe–C bonds. This is consistent with our previous MD simulations that showed chemisorption of TCP on iron oxide occurs predominantly through Fe–C bonding.[19,20] Therefore, the higher Fe/O ratio of Fe_3O_4 compared to Fe_2O_3 means that there are more Fe atoms available on the Fe_3O_4 surface for bonding. This is consistent with the nearly three times higher probability of the adsorption reaction pathway on Fe_3O_4 compared to Fe_2O_3 in Table 1. In contrast, more cresol is formed through non-adsorption reactions, including oligomerization, hydroxylation, and direct P–O bond dissociation on the Fe_2O_3 surface.

The Fe/O ratio of the two surfaces can also affect the hydroxylation and oligomerization pathways. These pathways, shown Fig. 5a and. 5c, involve reactions with OH whose oxygen atoms originate from the surface and H atoms either from the surface or the TCP molecules. During the surface preparation stage of our simulations, we found that 1.3 times more H/OH bonded to the Fe_2O_3 surface than the Fe_3O_4; see Fig S2. Therefore, more OH is available to participate in hydroxylation and oligomerization pathways on the Fe_2O_3 surface. This is reflected by the greater likelihood of these pathways in Table 1 for all cases except hydroxylation of mmm-TCP.

Lastly, MD simulations and GC-MS show that ppp-TCP is more reactive than mmm-TCP. The higher reactivity of ppp-TCP can be observed in Fig. S4, showing that a greater number of carbon atoms take part in the adsorption reaction. Also, the results show that, in contrast to mmm-TCP, which bonds to the surface primarily via the C5 and C6 atoms, ppp-TCP adsorbs through bonding with all of the carbon atoms in the cresyl ring. Comparing the relative frequency of the reaction pathways for the two isomers in Table 1, we observe that m-cresol forms mostly from the hydroxylation pathway whereas p-cresol is most often the product of the oligomerization pathway. The origin of this difference was investigated in terms of the energetics of the reaction pathways using NEB.

Energy Barriers

NEB was used to calculate the energy barrier for the rate-limiting step of each pathway for both mmm-TCP and ppp-TCP. The adsorption pathway was analyzed on both oxide surfaces. For the hydroxylation, adsorption and oligomerization pathways, the initial and final images used in the NEB calculation were taken directly from the dynamic simulations. The initial and final images for the direct dissociation reactions were created using QuantumATK. The NEB-predicted energy profiles for the P–O bond dissociation step of the hydroxylation reaction pathway for mmm-TCP and ppp-TCP are shown in Fig. 6. Clearly, the energy barrier for this step of the reaction is lower for ppp-TCP than for mmm-TCP.
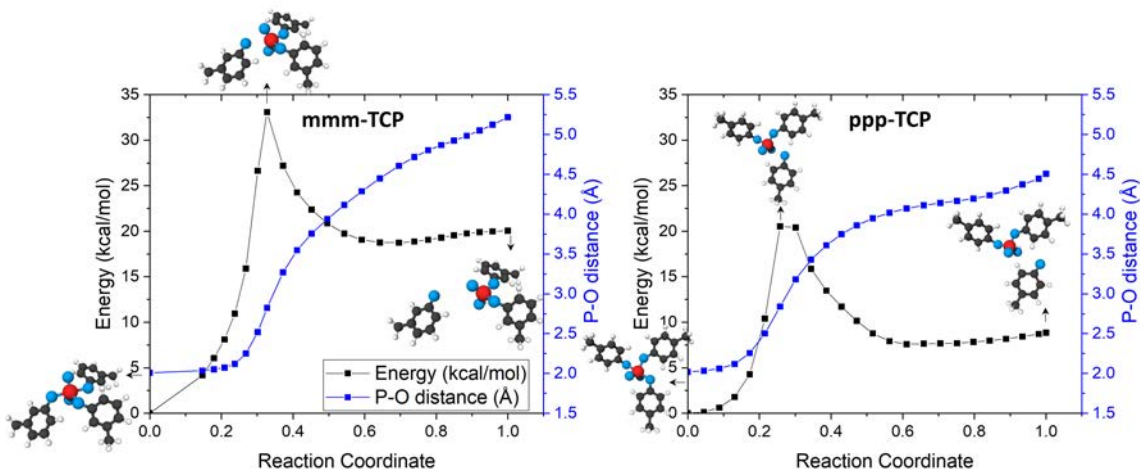
Figure 6: Energy profiles and corresponding P-O distance for the P-O bond dissociation step of the hydroxylation reaction pathway calculated using NEB. The NEB-predicted energy barrier for mmm-TCP is about 13 kcal/mol higher than for ppp-TCP. The insets show snapshots of the initial, saddle point and final replicas. The atom color scheme is the same as in Fig. 5

A similar analysis was performed for the adsorption and direct P-O dissociation pathways, for both isomers and, in the case of adsorption, both surfaces. The resultant NEB-calculated energy barriers are reported in Table 2. The barrier for the oligomerization pathway was in the range of 45 to 76 kcal/mol but could not be isolated further since each oligomerization reaction was involving slightly different chemical species. Considering the data in Table 2, the energy barrier for direct dissociation is higher than those for adsorption and hydroxylation, as expected. The lowest energy barrier, 20.5 kcal/mol, was obtained for ppp-TCP and the hydroxylation reaction pathway.

The energy barrier for the adsorption pathway was slightly lower than for the hydroxylation pathway for mmm-TCP but higher for ppp-TCP. The rate-limiting step for the adsorption pathway, however, is the adsorption of TCP on the surface through the creation of Fe–C bonds. The energy barrier for that step is always higher than the P–O bond dissociation step and the magnitude of the energy barrier for adsorption differs depending on the surface, isomer, and number of Fe–C or Fe–O bonds created. One NEB calculation predicted the energy barrier of the adsorption step to be about 65 kcal/mol for mmm-TCP

23

Table 2: Energy barriers for different reaction pathways leading to cresol formation calculated from NEB. All energies reported in kcal/mol. The oligomerization pathway is not shown since the energy barrier for that pathway depended on the chemical composition of the oligomer.

	mmm-TCP	ppp-TCP
Hydroxylation	31.7	20.5
Adsorption on Fe_2O_3	28.3	27.9
Adsorption on Fe_3O_4	28.6	25.8
Direct P-O Dissociation	76.7	75.8

on Fe_3O_4 surface. The higher energy barrier for Fe–C or Fe–O bond formation inhibited cresol formation through the adsorption pathway which is why there are only a few cases of adsorption pathway reported in Table 1.

Another general trend in Table 2 is that ppp-TCP energy barriers are lower than mmm-TCP energy barriers, especially for the hydroxylation reaction pathway. The approximately 13 kcal/mol lower energy barrier for ppp-TCP hydroxylation pathway compared to mmm-TCP is a key reason for the higher reactivity of ppp-TCP that was observed both in the GC-MS experiments and the reactive simulations. The difference between mmm-TCP and ppp-TCP must be attributable to their different structures. Note that the energy barriers calculated from NEB are based on the empirical ReaxFF interaction model.[19,48,49] So, although trends are likely to be correct since the force field was parameterized for a similar model system,[49] an empirical model-based approach cannot always be used to calculate energy barriers,[41] and ab initio calculations would be required to provide quantitative validation.

To understand how the structural differences between the two isomers affect the energy barrier for dissociation, the rotation of the dissociating cresol ring during the hydroxylation pathway was analyzed. This process was quantified as the angle of rotation around the P–O, O–C1 and C3–C4 axes, as illustrated in Fig. 7. The calculated angles for ppp-TCP shown in Fig. 7b are very different from those for mmm-TCP in Fig. 7c. Specifically, all three angles increased rapidly at the onset of the bond dissociation for mmm-TCP. A simultaneous initial

steep increase can also be seen in the energy profile of the mmm-TCP hydroxylation pathway in Fig. 6. Within the initial 0.2 Å change of the P-O distance, the energy went up to about 13 kcal/mol. This suggests that more energy was expended to rotate the m-cresol than to stretch the P–O bond at the beginning of the reaction. On the other hand, p-cresol rotated less than 5° around any of the axes, indicating that no extra rotation is required to facilitate the dissociation reaction of p-cresol.
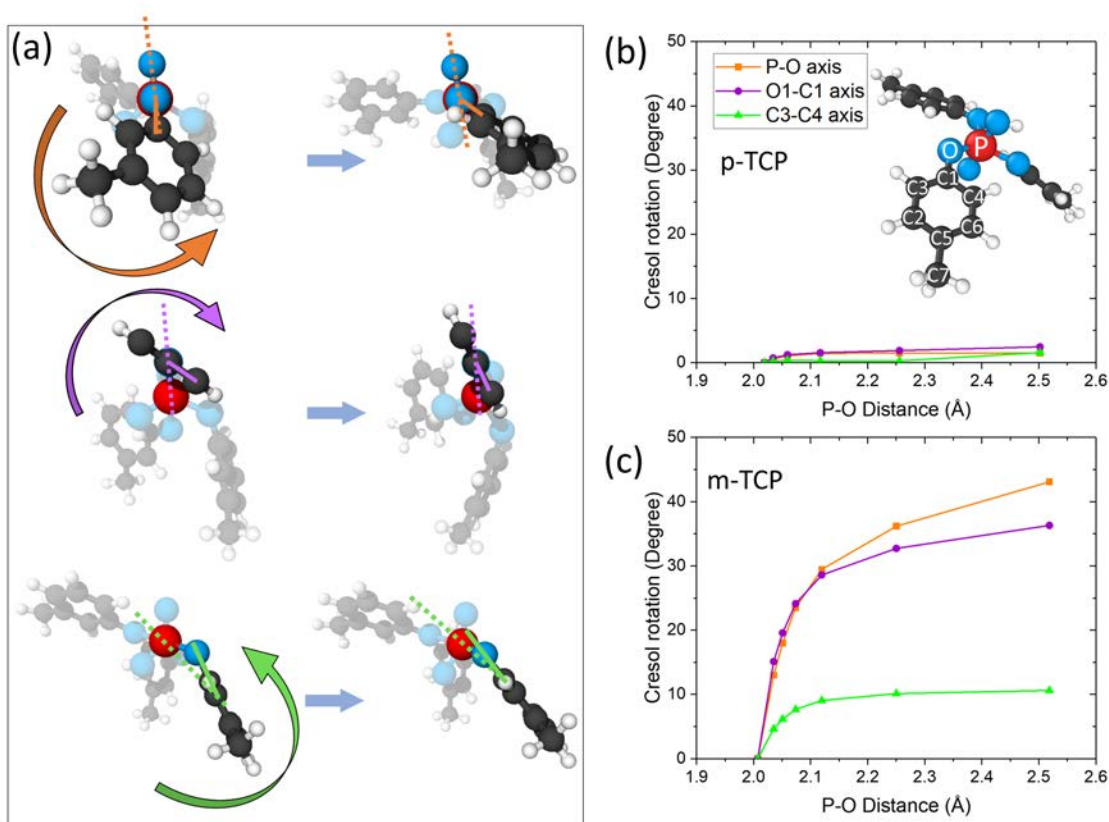

Figure 7: Rotation of the cresol ring as it moves away from the TCP molecule in NEB calculations. (a) Illustrations of the angles of rotation around P-O axis, O-C1 axis and C3-C4 axis, from top to bottom image. Snapshots on the left side are taken from the initial replicas and those on the right are from 7th replica for rotation around P-O bond and from 5th replica for the other two. Since cresol is a planar molecule, only the top half of the cresol ring is shown for rotation around the O-C1 axis to provide an unobstructed view of the rotation. Angles of rotation during the reaction are shown for (b) ppp-TCP and (c) mmm-TCP as a function of P-O distance.

Conclusions

In this study, we combined TPRS and GC-MS experiments with reactive MD simulations to study the thermal decomposition of TCP on ferrous surfaces. The investigation particularly focused on surface chemistry and TCP isomers, both of which can affect the decomposition rates and pathways. The TPRS experiments performed in air and nitrogen environments using a mixture of TCP isomers on Fe, Fe_3O_4, and Fe_2O_3 powders identified cresol as the main product of TCP decomposition. Further, characterization of the pyrolysis products using GC-MS experiments showed that reactivity trended as para-TCP > meta-TCP and Fe_2O_3 > Fe > Fe_3O_4. Reactive MD simulations captured the decomposition of TCP and tracked the formation of all reaction products, including oligomers, tolyl-TCP, cresol and toluene. Consistent with both sets of experiments, cresol was the predominant reaction product. Moreover, consistent with the GC-MS, the simulations showed that ppp-TCP is more reactive than mmm-TCP.

The simulations identified three primary reaction pathways leading to cresol formation: adsorption, oligomerization and hydroxylation. A statistical analysis was performed to determine the relative likelihood of each pathway. The statistical analysis was compared qualitatively to the GC-MS reactivity trends on the different oxide surfaces. The results were explained in terms of the availability of Fe on the surface for the adsorption pathway and OH released from the surface for the hydroxylation and oligomerization pathways. The higher reactivity of ppp-TCP compared to mmm-TCP isomers was explained by lower energy barriers for the ppp-TCP decomposition in NEB calculations. The energy difference was correlated to the energy needed to rotate the m-cresol for dissociation to occur via the hydroxylation pathway.

The subject of this study is directly relevant to phosphate-based antiwear additives and ferrous surfaces present in many industrial applications, particularly in aviation. Therefore, the relative reactivity of TCP isomers and the role of surface chemistry presented here can potentially be leveraged to design more effective antiwear additives that provide better

surface protection and ultimately improve the energy efficiency and useful lifetime of moving mechanical components. Further, the results have more general implications for fundamental understanding of how both the chemical composition of reactants and surface chemistry affect decomposition reactions.

Supporting Information Snapshots of the two model systems, changes in the number of adsorbed atoms during the hydroxylation process, comparison between the number of cresol groups produced from mmm-TCP and ppp-TCP, statistical analysis of bonding between mmm-TCP and ppp-TCPisomers.

References

(1) Arora, P.; Singh, R.; Seshadri, G.; Tyagi, A. K. Synthesis, Properties and Applications of Anionic Phosphate Ester Surfactants: A Review. *Tenside, Surfactants, Deterg.* **2018**, *55*, 266–272.

(2) Guan, B.; Pochopien, B. A.; Wright, D. S. The Chemistry, Mechanism and Function of Tricresyl Phosphate (TCP) as an Anti-Wear Lubricant Additive. *Lubr. Sci.* **2016**, *28*, 257–265.

(3) Johnson, D. W.; Hils, J. E. Phosphate Esters, Thiophosphate Esters and Metal Thio-phosphates as Lubricant Additives. *Lubricants* **2013**, *1*, 132–148.

(4) Spikes, H. Low- and Zero-Sulphated Ash, Phosphorus and Sulphur Anti-Wear Additives for Engine Oils. *Lubr. Sci.* **2008**, *20*, 103—-136.

(5) Godfrey, D. The Lubrication Mechanism of Tricresyl Phosphate on Steel. *ASLE Trans.* **1965**, *8*, 1–11.

(6) Faut, O. D.; Wheeler, D. R. On the Mechanism of Lubrication by Tricresylphosphate (TCP)—the Coefficient of Friction as a Function of Temperature for TCP on M-50 Steel. *ASLE Trans.* **1983**, *26*, 344–350.

(7) Gauthier, A. H. J. M.; Montes, H.; Georges, J. M. Boundary Lubrication With Tricre-sylphosphate (TCP). Importance of Corrosive Wear. *ASLE Trans.* **1982**, *25*, 445–455.

(8) Saba, C. S.; Forster, N. H. Reactions of Aromatic Phosphate Esters With Metals and Their Oxides. *Tribol. Lett.* **2002**, *12*, 135–146.

(9) Johnson, D. W.; Morrow, S.; Forster, N. H.; Saba, C. S. Vaporphase Lubrication: Reaction of Phosphate Ester Vapors With Iron and Steel. *Chem. Mater.* **2002**, *14*, 3767—-3775.

(10) Osei-Agyemang, E.; Berkebile, S.; Martini, A. Decomposition Mechanisms of Anti-wear Lubricant Additive Tricresyl Phosphate on Iron Surfaces Using DFT and Atomistic Thermodynamic Studies. *Tribol. Lett.* **2018**, *66*, 48.

(11) Phillips, W. D.; Rudnick, L. R. Ashless Phosphorus-containing Lubricating Oil Addi-tives. *Lubricant additives-chemisty and applications* **2009**, *124*, 63–121.

(12) Cho, L.; Klaus, E. E. Oxidative Degradation of Phosphate Esters. *ASLE Trans.* **1981**, *24*, 119–124.

(13) Sung, D.; Gellman, A. J. The Surface Chemistry of Alkyl and Arylphosphate Vapor Phase Lubricants on Fe Foil. *Tribology international* **2002**, *35*, 579–590.

(14) Rossi, A.; Piras, F. M.; Kim, D.; Gellman, A.; Spencer, N. Surface Reactivity of Tributyl Thiophosphate: Effects of Temperature and Mechanical Stress. *Tribol. Lett.* **2006**, *23*, 197–208.

(15) Sung, D.; Gellman, A. J. Thermal Decomposition of Tricresylphosphate Isomers on Fe. *Tribol. Lett.* **2002**, *13*, 9–14.

(16) Gao, F.; Kotvis, P. V.; Stacchiola, D.; Tysoe, W. T. Reaction of Tributyl Phosphate With Oxidized Iron: Surface Chemistry and Tribological Significance. *Tribol. Lett.* **2005**, *18*, 377–384.

(17) Mangolini, F.; Rossi, A.; Spencer, N. D. Reactivity of Triphenyl Phosphorothionate in Lubricant Oil Solution. *Tribol. Lett.* **2009**, *35*, 31–43.

(18) Ewen, J. P.; Latorre, C. A.; Khajeh, A.; Moore, J. D.; Remias, J.; Martini, A.; Dini, D. Substituent Effects on the Thermal Decomposition of Phosphate Esters on Ferrous Surfaces. *J. Phys. Chem. C* **2020**, *124*, 9852—-9865.

(19) Khajeh, A.; Hu, X.; Mohammadtabar, K.; Shin, Y. K.; van Duin, A. C.; Berkebile, S.; Martini, A. Statistical Analysis of Tri-cresyl Phosphate Conversion on an Iron Oxide Surface Using Reactive Molecular Dynamics Simulations. *J. Phys. Chem. C* **2019**, *123*, 12886–12893.

(20) Khajeh, A.; Krim, J.; Martini, A. Synergistic Effect of Nanodiamonds on the Adsorption of Tricresyl Phosphate on Iron Oxide Surfaces. *Appl. Phys. Lett.* **2019**, *114*, 171602.

(21) Zhang, L.; van Duin, A. C. T.; Zybin, S. V.; Goddard III, W. A. Thermal Decomposition of Hydrazines From Reactive Dynamics Using the ReaxFF Reactive Force Field. *J. Phys. Chem. B* **2009**, *113*, 10770—-10778.

(22) Loehlé, S.; Righi, M. C. Ab Initio Molecular Dynamics Simulation of Tribochemical Reactions Involving Phosphorus Additives at Sliding Iron Interfaces. *Lubricants* **2018**, *6*, 31.

(23) Yansheng, M.; Liu, J.; Wu, Y.; Gu., Z. The Synergistic Effects of Tricresyl Phosphate Oil Additive With Chemico-Thermal Treatment of Steel Surfaces. *Lubr. Sci.* **1996**, *9*, 85—-95.

(24) Klaus, E.; Jeng, G.; Duda., J. A Study of Tricresyl Phosphate as a Vapor-delivered Lubricant. *Lubr. Eng.* **1989**, *45*, 717—-723.

(25) Wheeler, D. R.; Faut, O. D. The Adsorption and Thermal Decomposition of Tricresylphosphate (TCP) on Iron and Gold. *Surf. Sci.* **1984**, *18*, 106—-122.

(26) Evans, R. D.; More, K. L.; Darragh, C. V.; Nixon, H. P. Transmission Electron Microscopy of Boundary-Lubricated Bearing Surfaces. Part I: Mineral Oil Lubricant. *Tribol. Trans.* **2004**, *47*, 430—-439.

(27) Evans, R. D.; More, K. L.; Darragh, C. V.; Nixon, H. P. Transmission Electron Microscopy of Boundary-Lubricated Bearing Surfaces. Part II: Mineral Oil Lubricant With Sulfur- and Phosphorus-Containing Gear Oil Additives. *Tribol. Trans.* **2005**, *48*, 299–307.

(28) Olla, M.; Navarra, G.; Elsener, B.; Rossi, A. Nondestructive In-Depth Composition Profile of Oxy-Hydroxide Nanolayers on Iron Surfaces From ARXPS Measurement. *Surf. Interface Anal.* **2006**, *38*, 964–974.

(29) Johnson, D. W.; Morrow, S.; Forster, N. H.; Saba, C. S. Vapor-Phase Lubrication: Reaction of Phosphate Ester Vapors With Iron and Steel. *Chem. Mater.* **2002**, *14*, 3767–3775.

(30) Loehlé, S.; Righi, M. First Principles Study of Organophosphorus Additives in Boundary Lubrication Conditions: Effects of Hydrocarbon Chain Length. *Lubr. Sci.* **2017**, *29*, 485–491.

(31) Righi, M. C.; Loehlé, S.; de Barros Bouchet, M.; Philippon, D.; Martin, J. Trimethyl-Phosphite Dissociative Adsorption on Iron by Combined First-Principle Calculations and XPS Experiments. *RSC Adv.* **2015**, *5*, 101162–101168.

(32) Lias, S.; Bartmess, J.; Liebman, J.; Holmes, J.; Levin, R.; Mallard, W. Ion Energetics Data in NIST Chemistry WebBook, NIST Standard Reference Database Number 69. *National Institute of Standards and Technology, Gaithersburg MD* **2018**, *20899*.

(33) Van Duin, A. C.; Dasgupta, S.; Lorant, F.; Goddard, W. A. ReaxFF: a Reactive Force Field for Hydrocarbons. *The Journal of Physical Chemistry A* **2001**, *105*, 9396–9409.

(34) Plimpton, S. Fast Parallel Algorithms for Short-range Molecular Dynamics. *J. Comput. Phys.* **1995**, *117*, 1–19.

(35) Stukowski, A. Visualization and Analysis of Atomistic Simulation Data With OVITO – the Open Visualization Tool. *Model. Simul. Mater. Sc.* **2009**, *18*, 015012.

(36) Smidstrup, S.; Markussen, T.; Vancraeyveld, P.; Wellendorff, J.; Schneider, J.; Gunst, T.; Verstichel, B.; Stradi, D.; Khomyakov, P. A.; Vej-Hansen, U. G. et al. QuantumATK: An Integrated Platform of Electronic and Atomic-Scale Modelling Tools. *J. Phys. Condens. Matter* **2019**, *32*, 015901.

(37) Berne, B. J.; Ciccotti, G.; Coker, D. F. *Classical and Quantum Dynamics in Condensed Phase Simulations: Proceedings of the International School of Physics*; World Scientific, 1998.

(38) Henkelman, G.; Jónsson, H. Improved Tangent Estimate in the Nudged Elastic Band

Method for Finding Minimum Energy Paths and Saddle Points. *J. Chem. Phys.* **2000**, *113*, 9978–9985.

(39) Nakano, A. A Space–Time-Ensemble Parallel Nudged Elastic Band Algorithm for Molecular Kinetics Simulation. *Comput. Phys. Commun.* **2008**, *178*, 280–289.

(40) Petucci, J.; LeBlond, C.; Karimi, M.; Vidali, G. Diffusion, Adsorption, and Desorption of Molecular Hydrogen on Graphene and in Graphite. *J. Chem. Phys.* **2013**, *139*, 044706.

(41) Rafatijo, H. Computing Activation Energies of Non-Thermal Reactions. *Mol. Phys.* **2020**, 1–13.

(42) Henkelman, G.; Uberuaga, B. P.; Jónsson, H. A Climbing Image Nudged Elastic Band Method for Finding Saddle Points and Minimum Energy Paths. *J. Chem. Phys.* **2000**, *113*, 9901–9904.

(43) Stein, O.; Lin, Z.; Zhigilei, L. V.; Asscher, M. Selective Ablation of Xe From Silicon Surfaces: Molecular Dynamics Simulations and Experimental Laser Patterning. *J. Phys. Chem. A* **2011**, *115*, 6250–6259.

(44) Tait, S. L.; Dohnálek, Z.; Campbell, C. T.; Kay, B. D. N-alkanes on Pt (111) and on C (0001)/ Pt (111): Chain Length Dependence of Kinetic Desorption Parameters. *J. Chem. Phys* **2006**, *125*, 234308.

(45) Zubkov, T.; Smith, R. S.; Engstrom, T. R.; Kay, B. D. Adsorption, Desorption, and Diffusion of Nitrogen in a Model Nanoporous Material. II. Diffusion Limited Kinetics in Amorphous Solid Water. *J. Chem. Phys.* **2007**, *127*, 184708.

(46) Schittkowski, J.; Buesen, D.; Toelle, K.; Muhler, M. The Temperature-programmed Desorption of H2 From Cu/ZrO2. *Catal. Lett.* **2016**, *146*, 1011–1017.

(47) Landers, M.; Gilkes, R. J.; Wells, M. A. Rapid Dehydroxylation of Nickeliferous Goethite in Lateritic Nickel Ore: X-Ray Diffraction and TEM Investigation. *Clays Clay Miner.* **2009**, *57*, 751–770.

(48) Verlackt, C.; Neyts, E.; Jacob, T.; Fantauzzi, D.; Golkaram, M.; Shin, Y.; Van Duin, A.; Bogaerts, A. Atomic-scale Insight Into the Interactions Between Hydroxyl Radicals and DNA in Solution Using the ReaxFF Reactive Force Field. *New J. Phys.* **2015**, *17*, 103005.

(49) Yue, D.-C.; Ma, T.-B.; Hu, Y.-Z.; Yeon, J.; van Duin, A. C. T.; Wang, H.; Luo, J. Tribo-chemistry of Phosphoric Acid Sheared Between Quartz Surfaces: A Reactive Molecular Dynamics Study. *J. Phys. Chem. C* **2013**, *117*, 25604–25614.

Graphical TOC Entry
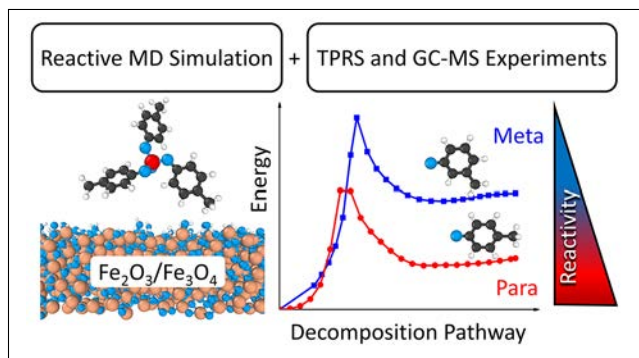
Thermal Decomposition of Tricresyl Phosphate on Ferrous Surfaces

Arash Khajeh,[†] Fakhrul H. Bhuiyan,[†] Jon-Erik Mogonye,[‡] Rose A.
Pesce-Rodriguez,[‡] Stephen Berkebile,[‡] and Ashlie Martini[*,†]

[†]Department of Mechanical Engineering, University of California Merced

[‡]U.S. Army Research Laboratory, Aberdeen Proving Ground
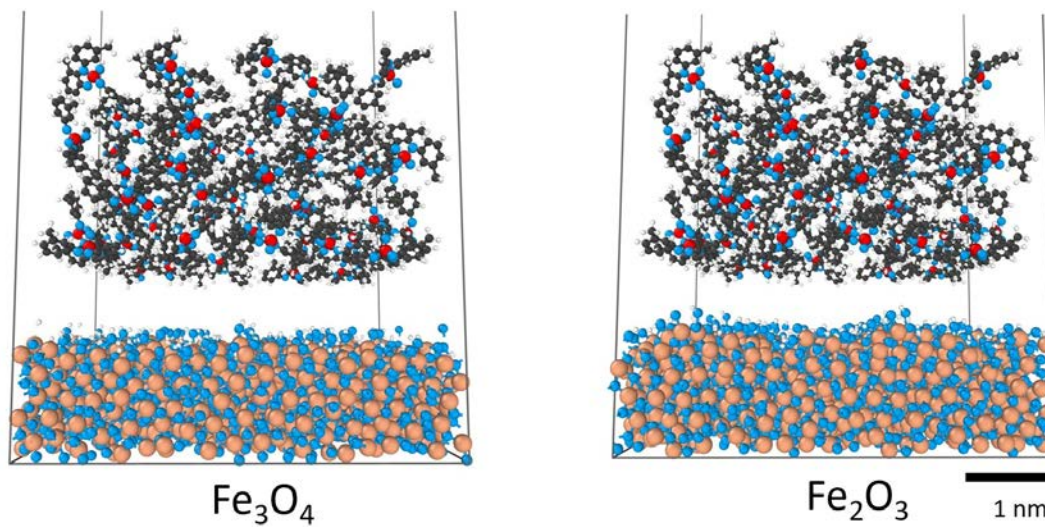
E-mail: amartini@ucmerced.edu

Supporting Information

Figure S1: Perspective view snapshots of the two model systems comprising 64 TCP molecules on OH passivated Fe_3O_4, and Fe_2O_3
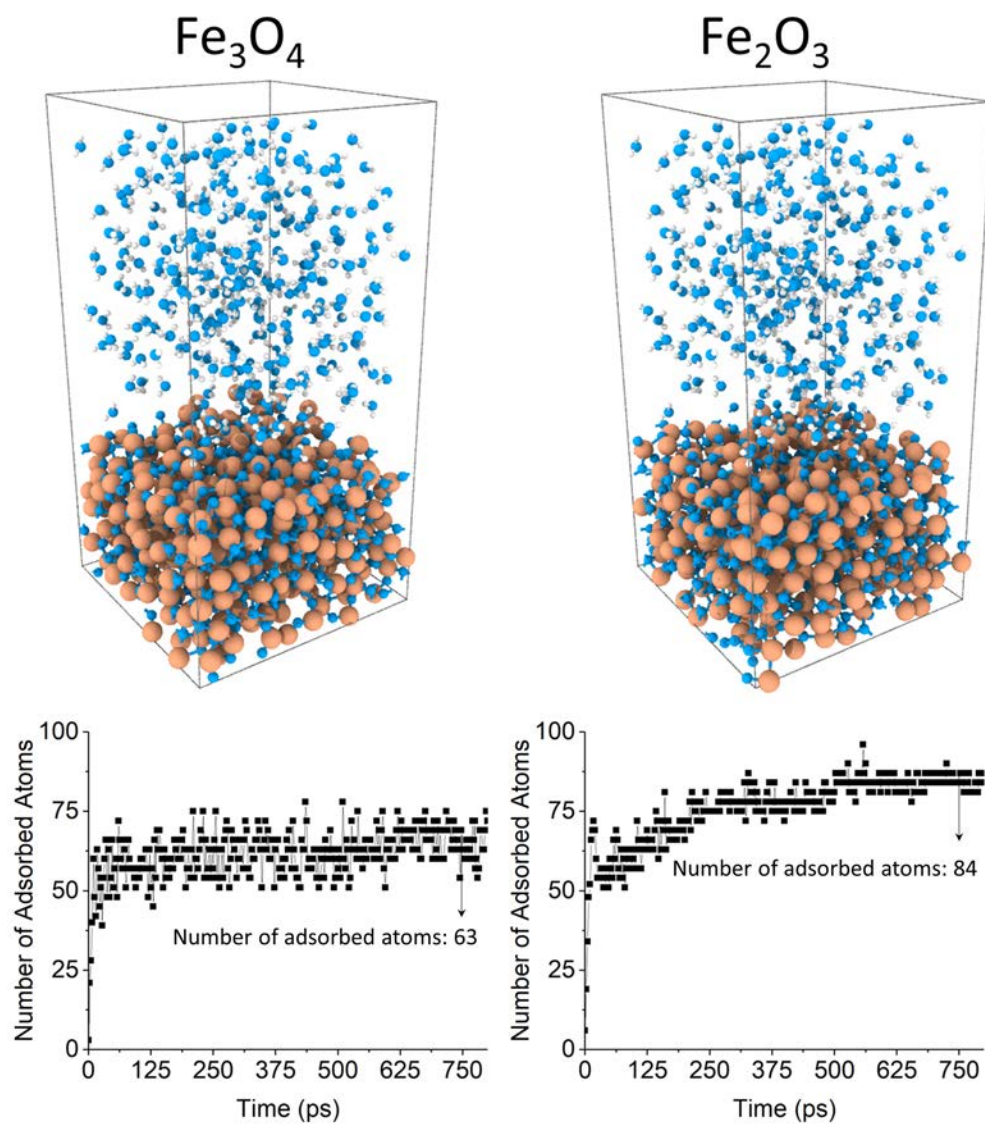
Figure S2: Change in the number of adsorbed atoms during the hydroxylation process for Fe_3O_4, and Fe_2O_3. The Fe_2O_3 surface bonded with 1.3 times more H/OH than the Fe_3O_4 surface.
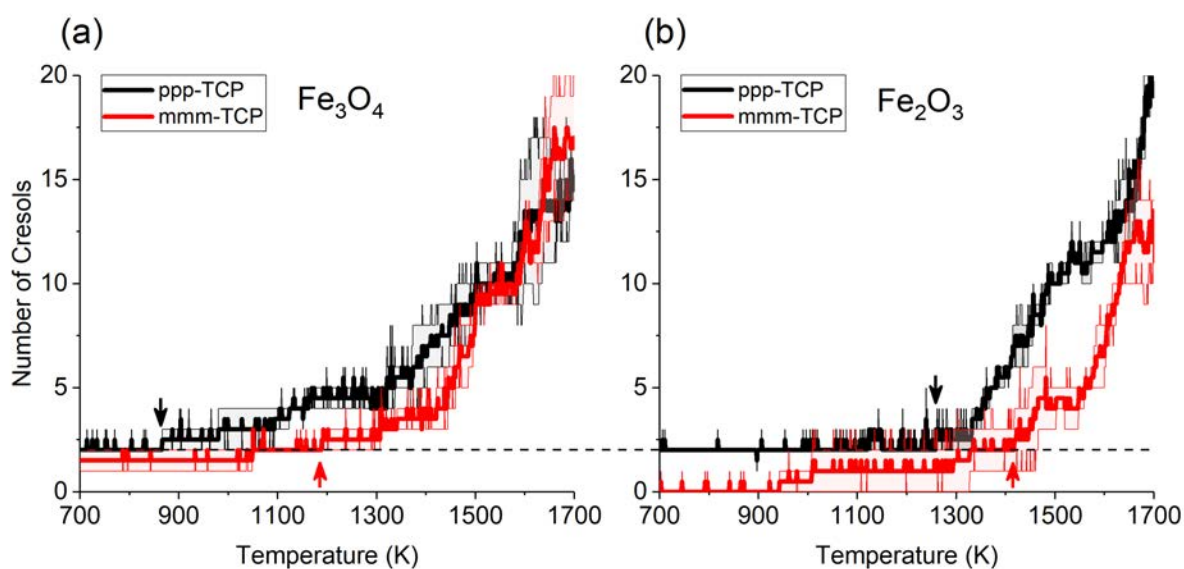
Figure S3: Comparison between the number of cresol groups produced from the decomposition of TCP in MD simulations with mmm-TCP and ppp-TCP on (a) Fe_3O_4 and (b) Fe_2O_3. The number of cresols from ppp-TCP is constantly higher than from mmm-TCP. The critical temperatures, identified by red and black arrows for ppp-TCP and mmm-TCP, respectively, correspond to the temperatures at which two cresols are first observed in the simulation.
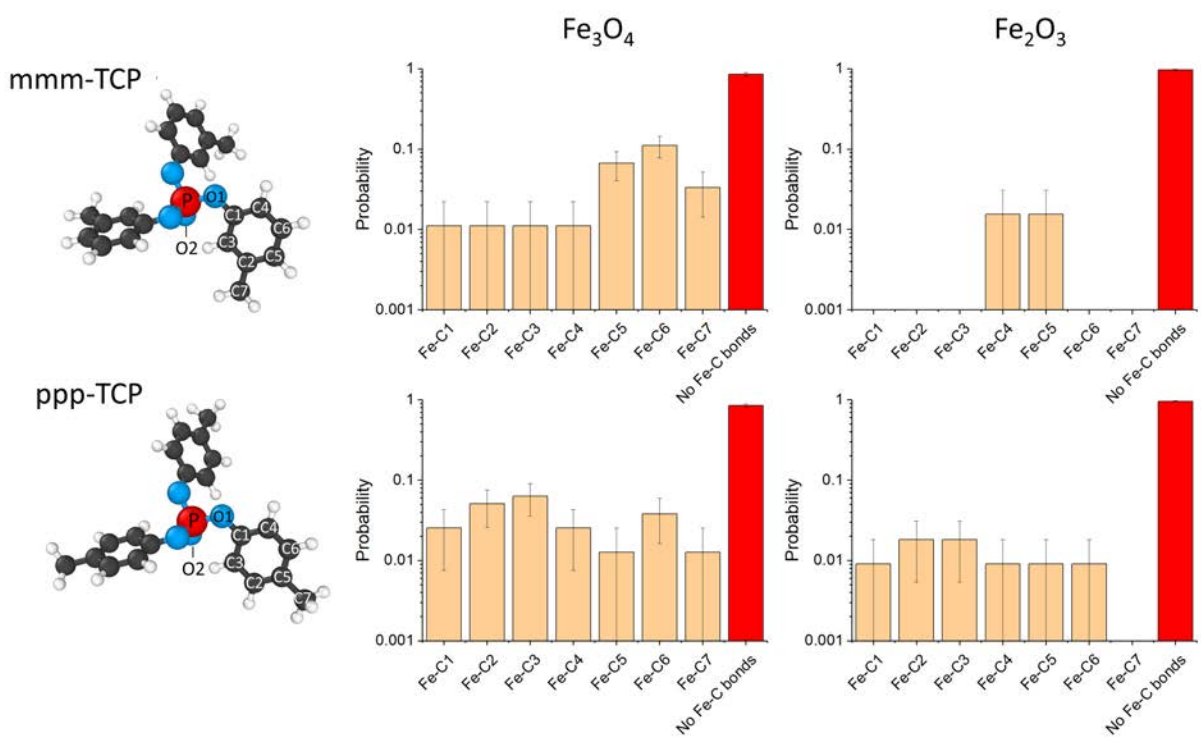
Figure S4: Statistical analysis of bonding between mmm-TCP (at the top) and ppp-TCP isomers (bottom) on Fe_3O_4 (left) and Fe_2O_3 surfaces (right) at the moment of cresol formation. Comparison between the two surfaces shows higher adsorption of ppp-TCP than mmm-TCP as well as a lower probability of TCP adsorption on the Fe_2O_3 surface that has the smaller Fe/O ratio. In all cases, most of the cresols form through non-adsorption reaction pathways.